A strongly cooperative spinel nanohybrid as an efficient bifunctional oxygen electrocatalyst for oxygen reduction reaction and oxygen evolution reaction

Ya-Qian Zhang[a], Meng Li[a], Bin Hua[a,*], Yue Wang[b], Yi-Fei Sun[a], Jing-Li Luo[a,*]

[a] Department of Chemical and Materials Engineering, University of Alberta, Edmonton, Alberta, T6G 1H9, Canada
[b] Department of Energy and Power Engineering, Tsinghua University, Beijing, 100084, China

ABSTRACT

The development of efficient, stable and low-cost bifunctional oxygen electrocatalysts is critical to the realization of practically viable rechargeable Zn-air batteries. Herein, we report a strongly cooperative spinel nanohybrid as a promising air electrode catalyst for rechargeable Zn-air batteries. Ultrafine sub-10 nm $MnFe_2O_4$ crystals are *in situ* grown on the ultrathin $NiCo_2O_4$ nanosheets, leading to a highly effective surface area and a strong synergistic chemical coupling effect. The distinct architecture and complex composition endow an excellent bifunctional oxygen electrocatalytic activity in alkaline condition. The practical rechargeable Zn-air battery with the hybrid electrocatalyst demonstrates a high round-trip efficiency (a low discharge-charge voltage gap of 0.81 V at a reversible current density of 10 mA cm^{-2}) and an outstanding durability, which outperforms the commercial Pt/Ru/C electrocatalyst. The resulting hybrid ($MnFe_2O_4/NiCo_2O_4$) shows great promise as an alternative bifunctional electrocatalyst to the precious metals for the application in Zn-air batteries.

1. Introduction

As a promising post lithium-ion technology, rechargeable Zn–air batteries have attracted intense attention in the past decades due to their high theoretical energy and power density [1,2]. However, the sluggish kinetics of the oxygen reduction/evolution reaction (ORR/OER) has been the technical hurdle for the Zn-air battery application [3]. Thus, the discovery of bifunctional electrocatalysts which could efficiently drive both ORR and OER is of paramount importance. Presently, the state-of-art bifunctional electrocatalysts are noble-metal based catalysts, such as Pt/RuO_2 or Pt/IrO_2. However, the commercialization of Zn-air battery is greatly hampered by two fundamental factors associated to the Pt/RuO_2 or Pt/IrO_2: (1) the high cost, scarcity of the noble metal, and (2) the poor stability of the electrocatalysts in cyclic charging/discharging environment [4–6]. Therefore, it is highly desirable yet challenging to design non-noble-metal-based bifunctional electrocatalysts with efficient catalytic activity and good stability.

Mixed-valence transition metal oxides have emerged as an alternative oxygen electrocatalyst, among which a two-dimensional $NiCo_2O_4$ nanosheets (NSs) electrocatalysts with an ultrathin feature has drawn particular interest owing to its excellent intrinsic OER activity, unique architecture, rich electroactive sites, and good electronic/ionic conductivity [7–12]. However, an insufficient ORR activity was found on $NiCo_2O_4$ electrocatalysts, which greatly limits their application in

rechargeable Zn-air batteries [13,14]. Therefore, considerable efforts are required to advance the bifunctionality of the $NiCo_2O_4$ NSs and to broaden their application in energy devices. Research has shown that assembling the ultrathin $NiCo_2O_4$ NSs with graphene leads to an enhanced catalytic activity derived from the synergetic chemical coupling effects between ultrathin NSs and foreign materials [15,16].

Herein, we report the *in situ* growth of ultrafine $MnFe_2O_4$ nanocrystals on ultrathin $NiCo_2O_4$ NSs (denoted as $MnFe_2O_4/NiCo_2O_4$) as a highly efficient and stable bifunctional electrocatalyst. Previous studies have shown that the spinel ferrite $MnFe_2O_4$ is highly active towards ORR; research conducted by Sun et al demonstrates that the monodispersed $MnFe_2O_4$ nanoparticles (NPs) supported on carbon support exhibits competitive ORR activity to the commercial Pt/C catalyst [17–19]. In an endeavor to boost the bifunctionality, sub-10 nm $MnFe_2O_4$ nanocrystals have been grown on $NiCo_2O_4$ ultrathin NSs. The ultrathin NS structure of $NiCo_2O_4$ affords a high specific surface area and sufficient anchoring sites that allow subsequent integration of highly dispersed NPs. This structure enables an intimate contact between $MnFe_2O_4$ NPs and $NiCo_2O_4$ NSs, which is attributed to an efficient utilization of the catalyst surface and an extended electrochemically active surface area. The significantly enhanced bifunctional oxygen electrocatalytic activity is credited to the distinct architecture and complex composition of the $MnFe_2O_4/NiCo_2O_4$ hybrid. The $MnFe_2O_4/NiCo_2O_4$ hybrid electrocatalyst exhibits an overpotential of

0.344 V at 10 mA cm^{-2} for the OER, and a positive half-wave potential of 0.767 V (vs. reversible hydrogen electrode, RHE) for the ORR. More importantly, the rechargeable Zn-air batteries employing the MnFe$_2$O$_4$/NiCo$_2$O$_4$ hybrid achieve a high round-trip efficiency with a low discharge − charge voltage gap of 0.81 V at a reversible current density of 10 mA cm^{-2} as well as an excellent durability over 100 cycles.

2. Results and discussions

The ultrathin NiCo$_2$O$_4$ NSs were firstly synthesized through a p-aminobenzoic acid (PABA) intercalation method, followed by a subsequent thermal treatment [7,8]. The as-synthesized NiCo$_2$O$_4$ NSs exhibit negative zeta potentials in neutral and alkaline media (Fig. S1). The integration of MnFe$_2$O$_4$ NPs on NiCo$_2$O$_4$ NSs was achieved using a non-hydrolytic thermal decomposition method with Mn(acac)$_2$ and Fe(acac)$_3$ as the sources, and oleylamine as the solvent and stabilizer [20]. Subsequently, the negatively charged NiCo$_2$O$_4$ NSs were introduced into the solution, which act as heterogeneous nucleation sites for the growth of MnFe$_2$O$_4$ NPs, owing to the charge interaction of Fe^{3+} and Mn^{2+}. In this synthesis, the loading amount of MnFe$_2$O$_4$ NPs was controlled by tailoring the ratio of Fe(acac)$_3$ and Mn(acac)$_2$ to the NiCo$_2$O$_4$. The strong anchoring of MnFe$_2$O$_4$ resulted from the heterogeneous nucleation led to an interfacial interaction of MnFe$_2$O$_4$ NPs with the ultrathin NiCo$_2$O$_4$ NSs, which was expected to exhibit high electrocatalytic activity and durability for oxygen electrocatalysis. For comparison, monodispersed MnFe$_2$O$_4$ NPs and physically mixed composite MnFe$_2$O$_4$ + NiCo$_2$O$_4$ were also prepared.

The XRD pattern of the as-prepared electrocatalyst clearly demonstrates the formation of MnFe$_2$O$_4$/NiCo$_2$O$_4$ hybrid (Fig. 1a), where the peak positions and relative intensities of all diffraction peaks are well matched with those of the resulting MnFe$_2$O$_4$ NPs, NiCo$_2$O$_4$ NSs and

corresponding standard diffraction patterns (PDF #10-0319 and PDF #20-0781). The FESEM image of MnFe$_2$O$_4$/NiCo$_2$O$_4$ hybrid in Fig. 1b shows the layered flower-like structure assembled with interconnected ultrathin NiCo$_2$O$_4$ NSs. Fig. 1c and d confirm the architecture of the MnFe$_2$O$_4$/NiCo$_2$O$_4$ hybrid, where the NiCo$_2$O$_4$ NSs are well integrated with MnFe$_2$O$_4$ NPs. From the TEM images shown in Figs. S2 and S3, the thickness of an individual NiCo$_2$O$_4$ NS matrix is around 6–7 nm. As revealed by the Brunauer–Emmett–Teller (BET) analysis (Fig. S4), the MnFe$_2$O$_4$/NiCo$_2$O$_4$ hybrid possesses a specific surface area of 118.6 m^2 g^{-1} with substantial mesopores (similar to that of NiCo$_2$O$_4$ NSs, with 131.8 m^2 g^{-1}), suggesting negligible agglomeration of the hybrid after the incorporation of MnFe$_2$O$_4$ NPs. This undoubtedly makes the MnFe$_2$O$_4$/NiCo$_2$O$_4$ hybrid an excellent electrocatalyst with high surface area and abundant electroactive sites. The chemical compositions of the MnFe$_2$O$_4$/NiCo$_2$O$_4$ hybrid, NiCo$_2$O$_4$ ultrathin NS and MnFe$_2$O$_4$ NPs were also confirmed by energy dispersive X-ray (EDX) spectroscopy (Figs. S5–S7) and inductively coupled plasma-atomic emission spectroscopy (ICP-AES); Based on ICP-AES result, the loading amount of MnFe$_2$O$_4$ NPs was estimated to be 47.2 wt.% in the MnFe$_2$O$_4$/NiCo$_2$O$_4$ hybrid, consistent with the set ratio. Moreover, the STEM-EDX and atom-scale high resolution TEM (HRTEM) in Fig. 1d and e give better insights into the chemical composition and material structure. The elemental mappings of MnFe$_2$O$_4$/NiCo$_2$O$_4$ hybrid (Fig. 1d) show the homogenous distributions of Mn, Fe, Ni, Co, indicating that the ultrafine MnFe$_2$O$_4$ NPs are uniformly dispersed on NiCo$_2$O$_4$ NSs without deteriorating the structure and ultrathin feature of the NiCo$_2$O$_4$ NSs during the formation of MnFe$_2$O$_4$ NPs. As demonstrated, the exposed edges of NiCo$_2$O$_4$ NSs are the electroactive centers for the water oxidation reaction and could remarkably facilitate the reaction kinetics [16]. To this end, the HRTEM was conducted; the lattice fringes with a d spacing of 2.51 Å (Fig. S3) on clean exposed edge
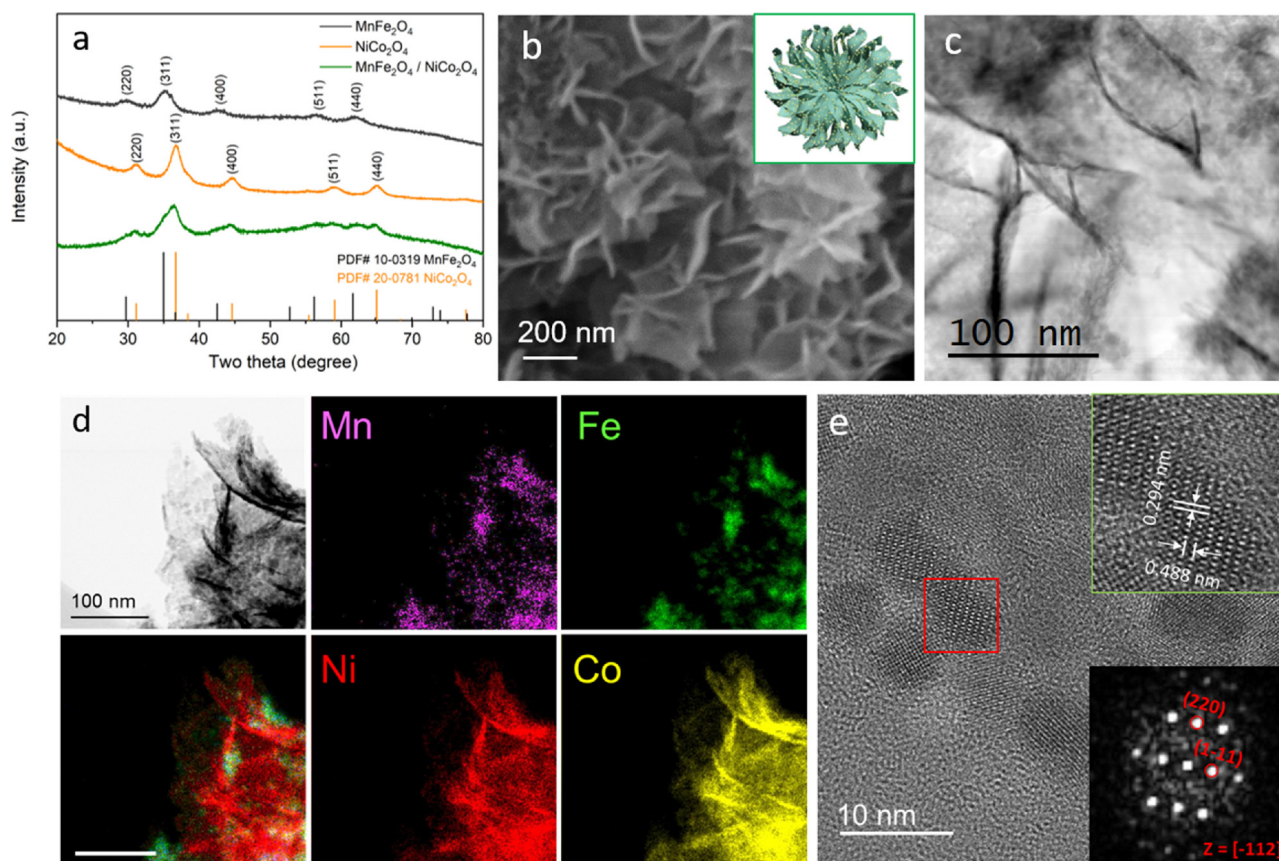
Fig. 1. (a) XRD of MnFe$_2$O$_4$ NPs, NiCo$_2$O$_4$ NSs and MnFe$_2$O$_4$/NiCo$_2$O$_4$ hybrid; (b) FESEM image and (c) TEM image of MnFe$_2$O$_4$/NiCo$_2$O$_4$ hybrid; (d) TEM image of MnFe$_2$O$_4$/NiCo$_2$O$_4$ hybrid with EDX mapping; (The scale bar is 100 nm) (e) HRTEM images of MnFe$_2$O$_4$ nanoparticles on NiCo$_2$O$_4$ NSs.
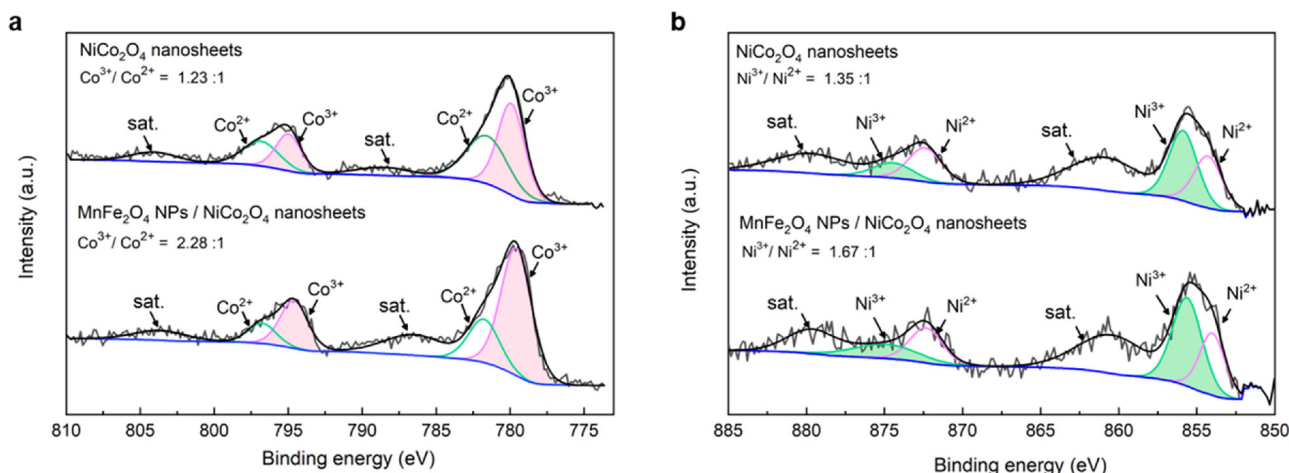
Fig. 2. The XPS profiles of $NiCo_2O_4$ NSs and $MnFe_2O_4/NiCo_2O_4$ hybrid. (a) Co 2p spectra and its simulations; (b) Ni 2p spectra and its simulations.

of $NiCo_2O_4$ NS were observed, which correspond to the (311) plane of $NiCo_2O_4$, implying that the $NiCo_2O_4$ is preferentially exposed with {311} facets [9]. As seen from Fig. 1e, the diameters of the NPs coupled on the $NiCo_2O_4$ are 5–7 nm. The HRTEM of $MnFe_2O_4/NiCo_2O_4$ hybrid, along with the corresponding diffractogram, shows the d spacings of 2.94 and 4.88 Å, indexed on the (220) and (1-11) planes of $MnFe_2O_4$. This HRTEM confirms that the non-hydrolytic synthetic method offers intriguing advantages to synthesize NPs with uniform size distribution and high crystallinity [20,21].

X-ray photoelectron spectroscopy (XPS) analysis was performed to study the electronic structure of Ni, Co, O in the $MnFe_2O_4/NiCo_2O_4$ hybrid and the ultrathin $NiCo_2O_4$ NSs. After loading with $MnFe_2O_4$ NPs, the Co 2p core level XPS spectra demonstrate that the electron binding energy of Co 2p experiences a decrease of ~ 0.4 eV. This is considered to accompany the oxidation of Co^{2+} to Co^{3+} [22]. The Co 2p core level spectra (Fig. 2a) were deconvoluted into two spin-orbit doublets, characteristic of Co^{2+} and Co^{3+}, and one shakeup satellite (identified as "Sat."). The deconvolution results manifest that, after loading with $MnFe_2O_4$ NPs, the ratio of Co^{3+} to Co^{2+} experienced a significant increase. It has been reported that Co^{3+} center plays a decisive role in determining H_2O adsorption, and consequently enabling high ORR and OER electrocatalytic activities [19,23]. As for the Ni 2p spectra (Fig. 2b), two spin orbit doublets, characteristic of Ni^{2+} and Ni^{3+} species, are found in both samples. The incorporated surface Ni^{3+} species also acts as the active sites to facilitate the OER [24].

Research has shown that the complex transition metal oxide generally results in complementary redox and beneficial electronic properties, and therefore is likely to show significant promise as electrocatalyst material [25]. As such, we investigated the bifunctional oxygen electrocatalytic performances of the $MnFe_2O_4/NiCo_2O_4$ hybrid for ORR and OER. The ORR electrocatalytic activities were first investigated by the cyclic voltammetry (CV) in O_2 and Ar saturated 0.1 M KOH, respectively. Using the $MnFe_2O_4/NiCo_2O_4$ hybrid, a more positive onset potential was achieved (Fig. S12), and the peak potential shifted from 0.695 V ($NiCo_2O_4$ NSs) to 0.770 V vs. Reversible Hydrogen Electrode (RHE). To reveal the ORR kinetics, the catalytic activity of the $MnFe_2O_4/NiCo_2O_4$ hybrid was further analyzed by the linear sweep voltammetry (LSV), using a rotating disk electrode (RDE) with different rotation speeds in O_2-saturated 0.1 M KOH. As benchmarks, the ORR catalytic activities of $MnFe_2O_4$ NPs, $NiCo_2O_4$ NSs and physically mixed composite as well as the commercial Pt/C electrocatalysts were evaluated. At 1600 rpm (Fig. 3a), the $NiCo_2O_4$ NSs showed a diffusion-limited current density of 4.66 mA cm^{-2} at 0.3 V (vs. RHE). The ORR E_{onset} and $E_{1/2}$ of the $NiCo_2O_4$ were 0.785 and 0.702 V, respectively. When coupled with $MnFe_2O_4$, the $MnFe_2O_4/NiCo_2O_4$ hybrid achieved a comparably higher catalytic ORR activity, with a more positive onset

potential (E_{onset} 0.881 V vs. RHE), half wave potential ($E_{1/2}$ 0.767 V), and higher diffusion-limited current density (5.01 mA cm^{-2} at 0.3 V). The physically mixed composite demonstrated a similar ORR electrocatalytic activity (Fig. S14), with an onset potential of 0.878 V and a half-wave potential of 0.783 V. It is suggested that the redox couple of Mn^{3+}/Mn^{2+} within the hybrid attributes to an enhanced ORR activity. As Mn^{2+} has a higher tendency to adsorb O_2, the surface redox active centers of $MnFe_2O_4$ presumably facilitate the O_2 adsorption and activation in the ORR [19,26]. With the onset potential of 0.912 V and half-wave potential of 0.835 V, $MnFe_2O_4$ NPs demonstrate the best ORR activity among the resulting spinel oxide catalysts, approaching to the commercial Pt/C catalyst performance wise. To further investigate the reaction kinetics of the hybrid for ORR, polarization curves were obtained on all samples at the rotating speeds of 400 to 2500 rpm (Fig. 3b and c, Figs. S10 and S11). The electron transfer numbers were estimated based on the slopes Koutecky-Levich equation at different potentials (ie., 0.3 V and 0.4 V). The electron transfer numbers (n) were calculated to be around 4.0 at 0.3–0.4 V for $MnFe_2O_4/NiCo_2O_4$ hybrid, slightly higher than that of $NiCo_2O_4$ NSs. This indicates that the electron transfer pathway is dominated by a four-electron route in the $MnFe_2O_4/NiCo_2O_4$ hybrid.

The LSV curves of the $MnFe_2O_4/NiCo_2O_4$ electrocatalyst for OER were measured at 1600 rpm in O_2 saturated 0.1 M KOH (Fig. 4a). Remarkably, the $MnFe_2O_4/NiCo_2O_4$ achieved the lowest overpotential of 344 mV at the current density of 10 mA cm^{-2}, significantly lower than that of $NiCo_2O_4$ NSs (456 mV). Of note, the $MnFe_2O_4$ NPs possess poor OER activity. Physically mixed composite, $MnFe_2O_4 + NiCo_2O_4$, also showed an improved OER catalytic activity (418 mV) as compared to the $NiCo_2O_4$ NSs. The remarkable OER activity of the $MnFe_2O_4/NiCo_2O_4$ hybrid mainly originated from the $NiCo_2O_4$ NSs, where $MnFe_2O_4$ served as a synergist. It is also worth noting that the $MnFe_2O_4/NiCo_2O_4$ hybrid outperforms the $MnFe_2O_4 + NiCo_2O_4$ composite, with the overpotential (at 10 mA cm^{-2}) being 74 mV lower than the $MnFe_2O_4 + NiCo_2O_4$ electrocatalyst (Fig. S15). It is deduced that the strong interfacial effects between $MnFe_2O_4$ NPs and $NiCo_2O_4$ NSs in the $MnFe_2O_4/NiCo_2O_4$ will contribute to a more efficient charge transfer between the NPs and the support NSs in comparison to the physically mixed composite [27]. The superb OER activity is also ascribed to the dual electroactive sites, i.e., the clean edge of the $NiCo_2O_4$ ultrathin NSs and the interfacial coupling sites between $MnFe_2O_4$ NPs and $NiCo_2O_4$ NSs.

Importantly, the $MnFe_2O_4/NiCo_2O_4$ hybrid demonstrated a smaller Tafel slope (46.7 mV dec^{-1}) than $NiCo_2O_4$ NSs (77.9 mV dec^{-1}) and $MnFe_2O_4$ NPs (115.5 mV dec^{-1}), as shown in Fig. 4b. A lower Tafel slope manifests a better OER activity as the electrode experiences smaller polarization upon increasing anodic current density [28].
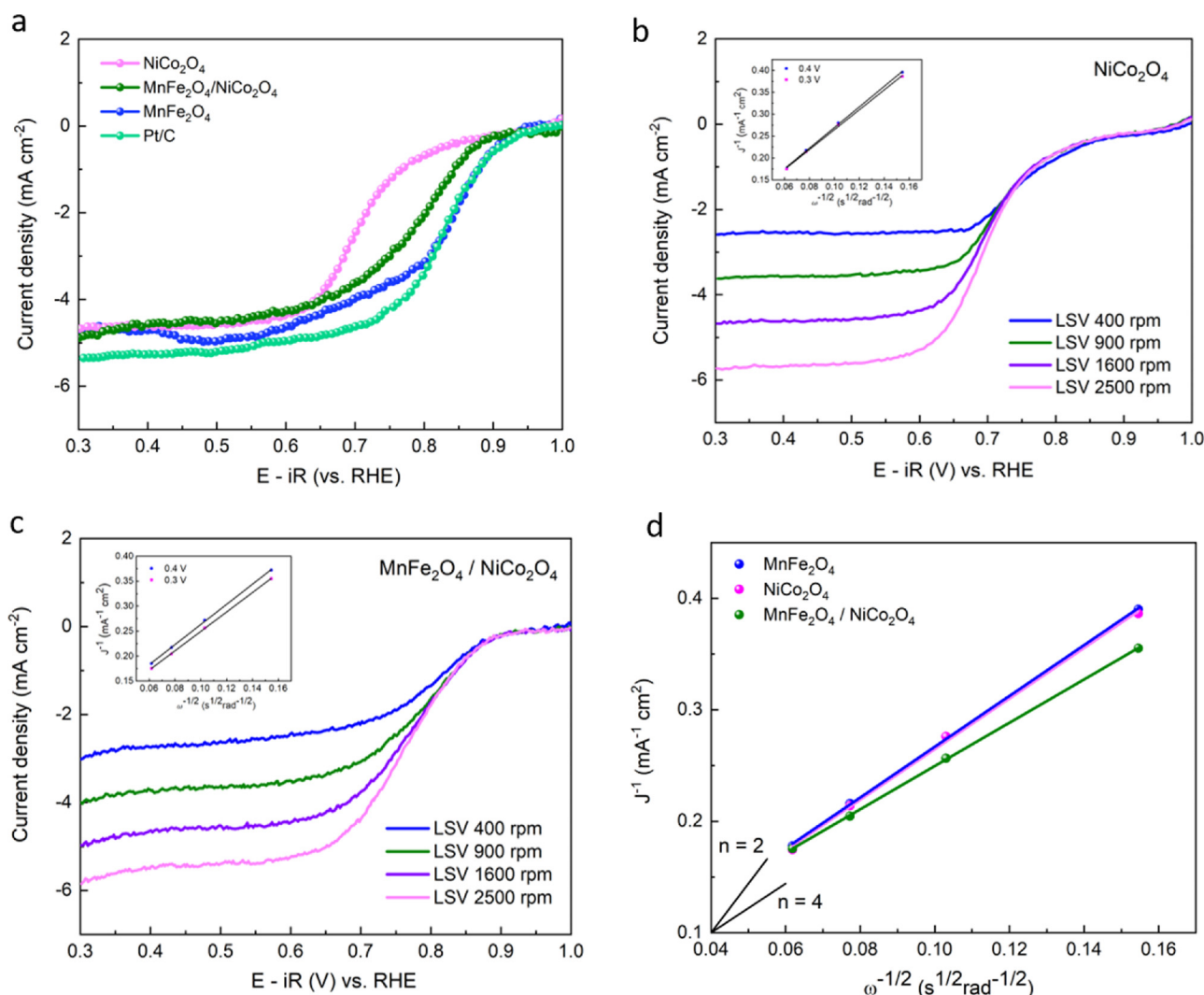
Fig. 3. (a) ORR LSV curves at 1600 rpm for $NiCo_2O_4$ NSs, $MnFe_2O_4$ NPs, $MnFe_2O_4/NiCo_2O_4$, and Pt/C. ORR LSV curves of (b) $NiCo_2O_4$ NSs and (c) $MnFe_2O_4/NiCo_2O_4$ hybrid in 0.1 M KOH at different rotation speeds (400, 900, 1600, and 2500 rpm). (d) Electron transfer number of $NiCo_2O_4$ NSs, $MnFe_2O_4$ NPs, $MnFe_2O_4/NiCo_2O_4$ derived from K–L plots at 0.3 V vs RHE.

Potentiostatic electrochemical impedance spectroscopy (EIS) conducted on $NiCo_2O_4$ ultrathin NSs and $MnFe_2O_4/NiCo_2O_4$ hybrid (Fig. 4c) further verifies the enhanced interfacial properties of the $MnFe_2O_4/NiCo_2O_4$ hybrid under the OER potential. For example, at a bias potential of 0.65 vs. Ag/AgCl, the $MnFe_2O_4/NiCo_2O_4$ hybrid shows an interfacial charge-transfer resistance of 3.73 Ω cm^2 (Table S1), dramatically lower than that of $NiCo_2O_4$ (15.68 Ω cm^2, Table S1). The simulated results indicate that the $MnFe_2O_4/NiCo_2O_4$ hybrid possesses a faster interfacial charge transfer process. A further enhanced charge-transfer process was found on the $MnFe_2O_4/NiCo_2O_4$ hybrid when 1 M KOH was used as the electrolyte (Fig. S17). Apart from the substantially enhanced electrocatalytic activity, the stability of the $MnFe_2O_4/NiCo_2O_4$ hybrid is also of great significance for the practical application [29]. To assess the stability, the galvanostatic long-term performances of $MnFe_2O_4/NiCo_2O_4$ were conducted at a constant current density load of 10 mA cm^{-2} in O_2-saturated 1 M KOH at 1600 rpm, as shown in Fig. S18. The OER potential of the $MnFe_2O_4/NiCo_2O_4$ hybrid was first plateaued at 1.56 V at a current density of 10 mA cm^{-2}, and the overpotential only experienced a 9 mV increase after polarized for 50 000 s. The overall bifunctional activity of the $MnFe_2O_4/NiCo_2O_4$ hybrid

was further confirmed by the potential difference between the OER potential of E_{10} and the ORR half-wave potential ($\Delta E = E_{10} - E_{1/2}$) in 0.1 M KOH. The bifunctional activities of the $MnFe_2O_4$ NPs, $NiCo_2O_4$ ultrathin NSs and Pt/Ru/C were also evaluated as shown in Fig. 4d. The $MnFe_2O_4/NiCo_2O_4$ hybrid shows the smallest potential difference (0.807 V) among the catalysts studied, and is comparable with many good bifunctional catalysts in alkaline conditions (Fig. 4e, listed in Table S2), which is indicative of the favorable bifunctionality of $MnFe_2O_4/NiCo_2O_4$. By integrating the $MnFe_2O_4$ NPs on the ultrathin $NiCo_2O_4$ NSs, the overall overpotential was successfully decreased by 177 mV.

On account of the architecture, chemical compositions and valence states of the $MnFe_2O_4/NiCo_2O_4$ hybrid, it is believed that the advanced bifunctionality is mainly attributed to the following two foundations. The uniform distribution of the ultrafine $MnFe_2O_4$ NPs on the porous ultrathin $NiCo_2O_4$ NSs results in a high electrolyte – material contact area and short ion diffusion paths, which facilitates the H_2O molecule adsorption and favors the charge-transfer [30,31]; the strong coupling of the $MnFe_2O_4$ NPs on the $NiCo_2O_4$ NSs suppresses the agglomeration of the nanoparticles during the long-term operation [27,32]. In
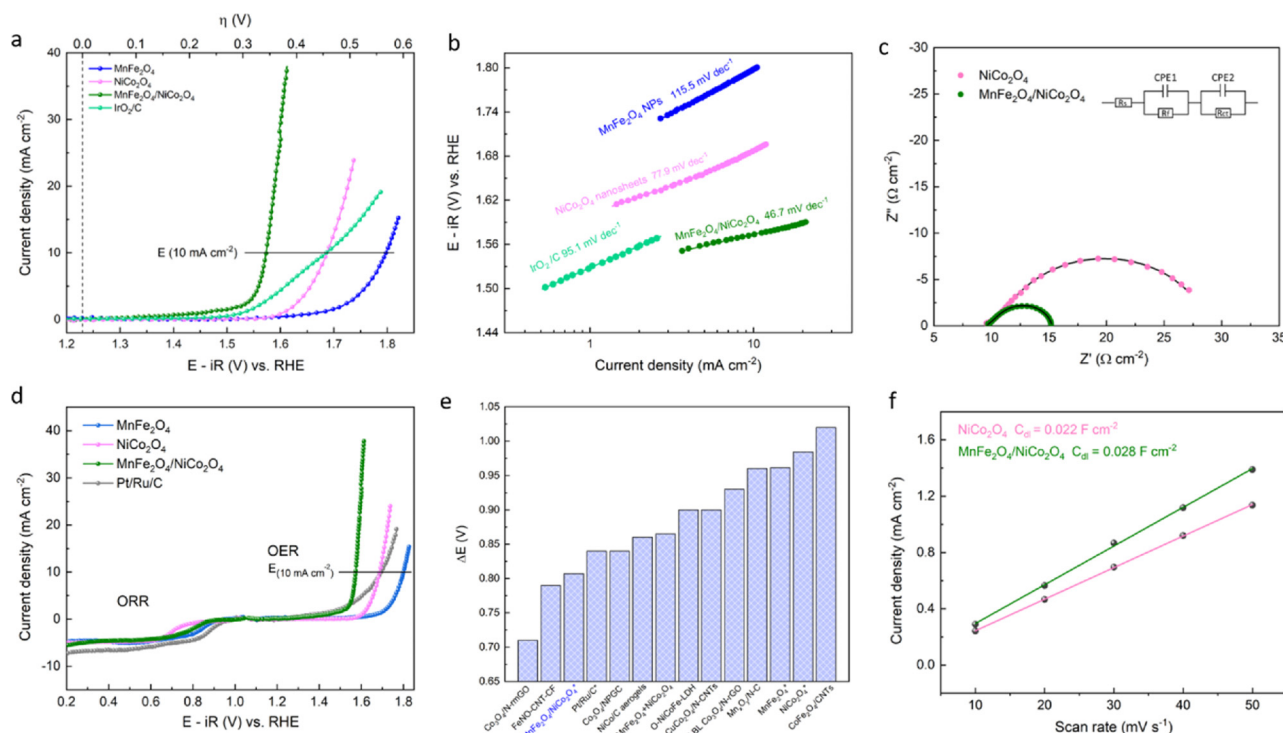
Fig. 4. LSV curves of (a) OER reaction on NiCo$_2$O$_4$ NSs, MnFe$_2$O$_4$ NPs, MnFe$_2$O$_4$/NiCo$_2$O$_4$, and IrO$_2$/C in 0.1 M KOH at 1600 rpm. (b) Tafel curves of on NiCo$_2$O$_4$ NSs, MnFe$_2$O$_4$ NPs, MnFe$_2$O$_4$/NiCo$_2$O$_4$, and IrO$_2$/C. (c) EIS curves of MnFe$_2$O$_4$/NiCo$_2$O$_4$ hybrid and NiCo$_2$O$_4$ NSs in 0.1 M KOH at a bias potential of 0.65 V vs. Ag/AgCl. Inset: equivalent circuit model for the Nyquist plots of the NiCo$_2$O$_4$ NSs and the MnFe$_2$O$_4$/NiCo$_2$O$_4$ hybrid electrocatalysts. (The R$_s$, R$_f$ and R$_{ct}$ represent the electrolyte, electrode film and charge transfer resistance, respectively. CPE1, CPE2 refer to the constant phase elements of the electrode film, and charge-transfer double-layer components.) (d) LSV curves of an overall oxygen reaction on MnFe$_2$O$_4$ NPs, NiCo$_2$O$_4$ NSs, MnFe$_2$O$_4$/NiCo$_2$O$_4$ hybrid and Pt/Ru/C. (e) The comparison of and overall overpotential for bifunctional electrocatalysts. (f) Measurements of the electrochemical double-layer capacitance of the NiCo$_2$O$_4$ NSs and the MnFe$_2$O$_4$/NiCo$_2$O$_4$ hybrid at current density at the potential of 1.275 V vs. scan rate.

addition, a lager electrochemical double layer capacitance was found on MnFe$_2$O$_4$/NiCo$_2$O$_4$, suggesting an extended electrochemical active surface area [33]. The capacitance of the double layer (C$_{dl}$) was evaluated by measuring the CV curves at a non-faradic potential range at different scan rates (Fig. 4f and S19) [34,35]; the C$_{dl}$ of MnFe$_2$O$_4$/NiCo$_2$O$_4$ is 0.028 F cm^{-2}, larger than that of NiCo$_2$O$_4$ (0.022 F cm^{-2}). This is likely to be one of the reasons for the enhanced electrocatalytic activity from the MnFe$_2$O$_4$/NiCo$_2$O$_4$ hybrid. This heterostructured hybrid realizes efficient bifunctional catalytic activities from the full utilization of the catalyst surface and strong interaction between the MnFe$_2$O$_4$ NPs and NiCo$_2$O$_4$ matrix. The decreased overall potential difference between ORR and OER on MnFe$_2$O$_4$/NiCo$_2$O$_4$ indicates a small energy loss in the charging/discharging process.

Building on bifunctional electrochemical activities studied above on the RDE electrode, the oxygen catalytic activity of the MnFe$_2$O$_4$/NiCo$_2$O$_4$ hybrid was further evaluated in the rechargeable Zn-air battery. As shown in Fig. 5a (see the photo in Fig. S20), a proof-of-concept rechargeable Zn-air battery was assembled with zinc plate as the anode, oxygen electrocatalyst coated gas diffusion layer (GDL) as the cathode. Fig. 5b shows typical discharge − charge polarization curves of the rechargeable Zn-air battery. The MnFe$_2$O$_4$/NiCo$_2$O$_4$ hybrid exhibits a discharge − charge voltage gap of 0.80 V at 10 mA cm^{-2} and 1.10 V at 50 mA cm^{-2}, which are significant lower than those of NiCo$_2$O$_4$ (0.94 V at 10 mA cm^{-2} and 1.28 V at 50 mA cm^{-2}) and commercial Pt/Ru/C catalyst (0.87 at 10 mA cm^{-2} and 1.25 V at 50 mA cm^{-2}). The small voltage gaps between charging and discharging processes on MnFe$_2$O$_4$/NiCo$_2$O$_4$ hybrid suggest an enhanced voltaic efficiency of the MnFe$_2$O$_4$/NiCo$_2$O$_4$ hybrid. More importantly, the hybrid catalyst exhibits

excellent durability with stable efficiency in Fig. 5c. When being repeatedly charged-discharged at a constant current density of 10 mA cm^{-2} (10 min charging, 10 min discharging), no observable degradation was found on the MnFe$_2$O$_4$/NiCo$_2$O$_4$ hybrid after 100 cycles. The voltaic efficiency was found to be 59.7% at the beginning and experienced a slight increase after 32 h of the operation (60.8%). In contrast, the Pt/Ru/C shows a much inferior stability during the charging-discharging process with the voltaic efficiency decreasing from 56.4% to 49.7%, caused by the passivation of Pt at positive potentials pertinent to OER and electrocatalyst detachment [4,36].

3. Conclusions

In summary, we reported a desirable approach to preparing an efficient bifunctional oxygen electrocatalyst through synergistically integrating non-precious metal oxide nanoparticles on ultrathin NSs. This inexpensive, earth-abundant hybrid catalyst exhibits superior bifunctional catalytic activity in terms of its lower overall overpotential (ΔE = 0.807 V) than the MnFe$_2$O$_4$ and NiCo$_2$O$_4$ electrocatalyst. The fact that the MnFe$_2$O$_4$/NiCo$_2$O$_4$ hybrid outperforms the state-of-the-art precious metals Pt/Ru/C with respect to bifunctional activity and durability makes the discovery in this study more promising. We believe that the large surface area, high chemical stability of NiCo$_2$O$_4$ NSs and strong chemical coupling effects between MnFe$_2$O$_4$ NPs and NiCo$_2$O$_4$ afford the enhanced bifunctional catalytic activity and durability. This work holds the promise to open a new possibility in designing novel transition metal based bifunctional catalysts as the alternatives to the noble metals for the application in energy related devices.
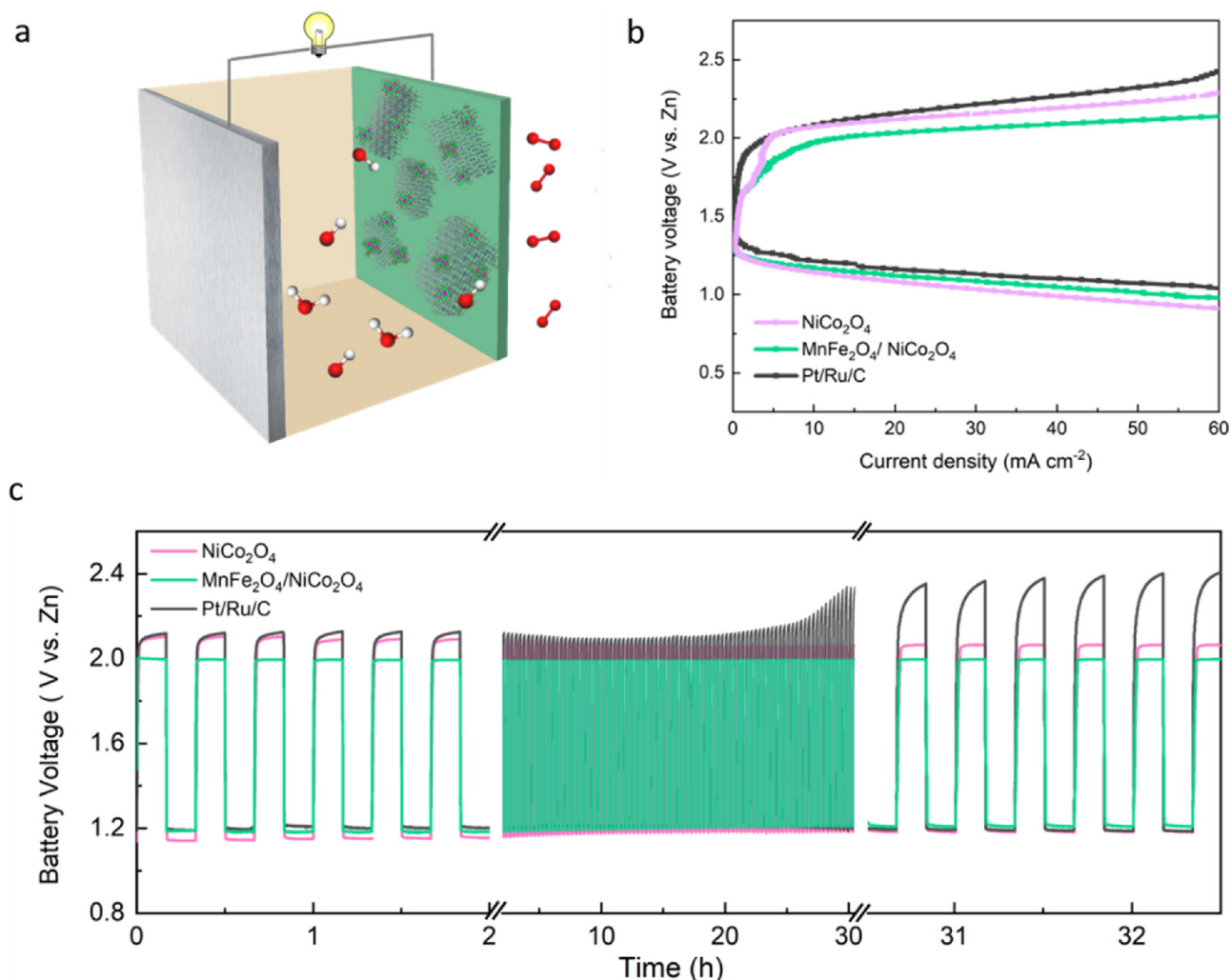
Fig. 5. (a)The schematic figure of the custom built rechargeable Zn − air batteries. (b) Charge and discharge polarization curves of NiCo$_2$O$_4$ NSs, MnFe$_2$O$_4$/NiCo$_2$O$_4$, and Pt/Ru/C air electrode. (c) Galvanostatic charge − discharge curves at 10 mA cm^{-2} using NiCo$_2$O$_4$ NSs, MnFe$_2$O$_4$/NiCo$_2$O$_4$, and Pt/Ru/C air electrode.

Acknowledgements

Appendix A. Supplementary data

Supplementary material related to this article can be found, in the online version, at doi: https://doi.org/10.1016/j.apcatb.2018.05.047.

References

[1] Y. Li, M. Gong, Y. Liang, J. Feng, J.E. Kim, H. Wang, G. Hong, B. Zhang, H. Dai, Advanced zinc-air batteries based on high-performance hybrid electrocatalysts, Nat. Commun. 4 (2013) 1805.

[2] X. Wang, Y. Li, T. Jin, J. Meng, L. Jiao, M. Zhu, J. Chen, Electrospun thin-walled CuCo$_2$O$_4$@ C nanotubes as bifunctional oxygen electrocatalysts for rechargeable Zn–air batteries, Nano Lett. 17 (2017) 7989–7994.

[3] X. Liu, M. Park, M.G. Kim, S. Gupta, G. Wu, J. Cho, Integrating NiCo alloys with their oxides as efficient bifunctional cathode catalysts for rechargeable zinc–air batteries, Angew. Chem. Int. Ed. 54 (2015) 9654–9658.

[4] J. Zhang, Z. Zhao, Z. Xia, L. Dai, A metal-free bifunctional electrocatalyst for oxygen reduction and oxygen evolution reactions, Nat. Nanotechnol. 10 (2015) 444–452.

[5] I.S. Amiinu, X. Liu, Z. Pu, W. Li, Q. Li, J. Zhang, H. Tang, H. Zhang, S. Mu, From 3D ZIF nanocrystals to Co–Nx/C nanorod array electrocatalysts for ORR, OER, and Zn–air batteries, Adv. Funct. Mater. 28 (2018) 1704638.

[6] M. Xiong, D.G. Ivey, Electrodeposited Co-Fe as an oxygen evolution catalyst for rechargeable zinc-air batteries, Electrochem. Commun. 75 (2017) 73–77.

[7] H.W. Wang, Z.A. Hu, Y.Q. Chang, Y.L. Chen, H.Y. Wu, Z.Y. Zhang, Y.Y. Yang, Design and synthesis of NiCo$_2$O$_4$–reduced graphene oxide composites for high performance supercapacitors, J. Mater. Chem. 21 (2011) 10504–10511.

[8] J. Bao, X. Zhang, B. Fan, J. Zhang, M. Zhou, W. Yang, X. Hu, H. Wang, B. Pan, Y. Xie, Ultrathin spinel-structured nanosheets rich in oxygen deficiencies for enhanced electrocatalytic water oxidation, Angew. Chem. Int. Ed. 127 (2015) 7507–7512.

[9] J. Yang, C. Yu, S. Liang, S. Li, H. Huang, X. Han, C. Zhao, X. Song, C. Hao, P.M. Ajayan, J. Qiu, Bridging of ultrathin NiCo$_2$O$_4$ nanosheets and graphene with polyaniline: a theoretical and experimental study, Chem. Mater. 28 (2016) 5855–5863.

[10] Y. Zhu, W. Zhou, Z. Shao, Perovskite/carbon composites: applications in oxygen electrocatalysis, Small 13 (2017) 1603793.

[11] Y. Zhu, W. Zhou, Y. Zhong, Y. Bu, X. Chen, Q. Zhong, M. Liu, Z. Shao, A perovskite nanorod as bifunctional electrocatalyst for overall water splitting, Adv. Energy Mater. 7 (2017) 1602122.

[12] S. Khilari, S. Pandit, D. Das, D. Pradhan, Manganese cobaltite/polypyrrole nanocomposite-based air-cathode for sustainable power generation in the single-chambered microbial fuel cells, Biosens. Bioelectron. 54 (2014) 534–540.

[13] G. Zhang, B.Y. Xia, X. Wang, Strongly coupled NiCo$_2$O$_4$-rGO hybrid nanosheets as a methanol-tolerant electrocatalyst for the oxygen reduction reaction, Adv. Mater. 26 (2014) 2408–2412.

[14] P. Moni, S. Hyun, A. Vignesh, S. Shanmugam, Chrysanthemum flower like NiCo$_2$O$_4$ -nitrogen doped graphene oxide composite: an efficient electrocatalyst for lithium-oxygen and zinc-air batteries, Chem. Commun. 53 (2017) 7836–7839.

[15] G. Gao, H.B. Wu, X.W. Lou, Citrate-assisted growth of NiCo$_2$O$_4$ nanosheets on reduced graphene oxide for highly reversible lithium storage, Adv. Energy Mater. 4 (2014) 1400422.

[16] S. Chen, S.Z. Qiao, Hierarchically porous nitrogen-doped graphene–NiCo$_2$O$_4$ hybrid paper as an advanced electrocatalytic water-splitting material, ACS Nano 7 (2013) 10190–10196.

[17] H. Zhu, S. Zhang, Y.X. Huang, L. Wu, S. Sun, Monodisperse $M_xFe_{3-x}O_4$ (M = Fe, Cu, Co, Mn) nanoparticles and their electrocatalysis for oxygen reduction reaction, Nano Lett. 13 (2013) 2947–2951.

[18] S. Khilari, S. Pandit, J.L. Varanasi, D. Das, D. Pradhan, Bifunctional manganese ferrite/polyaniline hybrid as electrode material for enhanced energy recovery in microbial fuel cell, ACS Appl. Mater. Interfaces 7 (2015) 20657–20666.

[19] S. Khilari, D. Pradhan, $MnFe_2O_4$@ nitrogen-doped reduced graphene oxide nano-hybrid: an efficient bifunctional electrocatalyst for anodic hydrazine oxidation and cathodic oxygen reduction, Catal. Sci. Technol. 7 (2017) 5920–5931.

[20] L. Pérez-Mirabet, E. Solano, F. Martínez-Julián, R. Guzmán, J. Arbiol, T. Puig, X. Obradors, A. Pomar, R. Yáñez, J. Ros, S. Ricart, One-pot synthesis of stable colloidal solutions of MFe_2O_4 nanoparticles using oleylamine as solvent and stabilizer, Mater. Res. Bull. 48 (2013) 966–972.

[21] P.D. Cozzoli, M.L. Curri, A. Agostiano, G. Leo, M. Lomascolo, ZnO nanocrystals by a non-hydrolytic route: synthesis and characterization, J. Phys. Chem. B. 10 (2003) 4756–4762.

[22] J.G. Kim, D.L. Pugmire, D. Battaglia, M.A. Langell, Analysis of the $NiCo_2O_4$ spinel surface with Auger and X-ray photoelectron spectroscopy, Appl. Surf. Sci. 165 (2000) 70–84.

[23] W. Song, Z. Ren, S.Y. Chen, Y. Meng, S. Biswas, P. Nandi, H.A. Elsen, P.X. Gao, S.L. Suib, Ni-and Mn-promoted mesoporous Co_3O_4: a stable bifunctional catalyst with surface-structure-dependent activity for oxygen reduction reaction and oxygen evolution reaction, ACS Appl. Mater. Interfaces 8 (2016) 20802–20813.

[24] H.Y. Wang, Y.Y. Hsu, R. Chen, T.S. Chan, H.M. Chen, B. Liu, Ni^{3+}-induced formation of active NiOOH on the spinel Ni–Co oxide surface for efficient oxygen evolution reaction, Adv. Energy Mater. 5 (2015) 1500091.

[25] A. Yu, Z. Chen, R. Maric, L. Zhang, J. Zhang, J. Yan, Electrochemical super-capacitors for energy storage and delivery: advanced materials, technologies and applications, Appl. Energy 153 (2015) 1–2.

[26] C.H. Choi, S.H. Park, S.I. Woo, Oxygen reduction activity of Pd–Mn_3O_4 nanoparticles and performance enhancement by voltammetrically accelerated degradation, Phys. Chem. Chem. Phys. 14 (2012) 6842–6848.

[27] Z. Xi, D.P. Erdosy, A. Mendoza-Garcia, P.N. Duchesne, J. Li, M. Muzzio, Q. Li, P. Zhang, S. Sun, Pd nanoparticles coupled to $WO_{2.72}$ nanorods for enhanced electrochemical oxidation of formic acid, Nano Lett. 17 (2017) 2727–2731.

[28] R.L. Doyle, M.E.G. Lyons, The oxygen evolution reaction: mechanistic concepts and catalyst design, in: S. Gimenez, J. Bisquert (Eds.), Photochemical Solar Fuel Production: From Basic Principles to Advanced Devices, Springer, Berlin, 2016, pp. 41–104.

[29] T.Y. Ma, S. Dai, M. Jaroniec, S.Z. Qiao, Metal–organic framework derived hybrid Co_3O_4-carbon porous nanowire arrays as reversible oxygen evolution electrodes, J. Am. Chem. Soc. 136 (2014) 13925–13931.

[30] A.S. Arico, P. Bruce, B. Scrosati, J.M. Tarascon, W. Van Schalkwijk, Nanostructured materials for advanced energy conversion and storage devices, Nat. Mater. 4 (2005) 366–377.

[31] J. Liu, J. Jiang, C. Cheng, H. Li, J. Zhang, H. Gong, H.J. Fan, Co_3O_4 nanowire@ MnO_2 ultrathin nanosheet core/shell arrays: a new class of high-performance pseudocapacitive materials, Adv. Mater. 23 (2011) 2076–2081.

[32] Y. Hou, S. Cui, Z. Wen, X. Guo, X. Feng, J. Chen, Strongly coupled 3D hybrids of N-doped porous carbon nanosheet/CoNi alloy-encapsulated carbon nanotubes for enhanced electrocatalysis, Small 11 (2015) 5940–5948.

[33] S. Jung, C.C. McCrory, I.M. Ferrer, J.C. Peters, T.F. Jaramillo, Benchmarking nanoparticulate metal oxide electrocatalysts for the alkaline water oxidation reaction, J. Mater. Chem. A. 4 (2016) 3068–3076.

[34] D. Merki, H. Vrubel, L. Rovelli, S. Fierro, X. Hu, Fe, Co, and Ni ions promote the catalytic activity of amorphous molybdenum sulfide films for hydrogen evolution, Chem. Sci. 3 (2012) 2515–2525.

[35] H. Hu, B. Guan, B. Xia, X.W. Lou, Designed formation of $Co_3O_4/NiCo_2O_4$ double-shelled nanocages with enhanced pseudocapacitive and electrocatalytic properties, J. Am. Chem. Soc. 137 (2015) 5590–5595.

[36] K.N. Jung, J.H. Jung, W.B. Im, S. Yoon, K.H. Shin, J.W. Lee, Doped lanthanum nickelates with a layered perovskite structure as bifunctional cathode catalysts for rechargeable metal–air batteries, ACS Appl. Mater. Interfaces 5 (2013) 9902–9907.